Research Square

Preprints are preliminary reports that have not undergone peer review.
They should not be considered conclusive, used to inform clinical practice,
or referenced by the media as validated information.

Interfacial Engineering of Si@SiOx with an N-Doped Carbon Shell for High-Performance Lithium-Ion Battery Anodes

Bowen Li
Ningxia Research Center of Silicon-Target and-Silicon-Carbon Negative Materials Engineering Technology, North Minzu University

Haidong Xie
Fuzhou University

Hui Tian
Ningxia Research Center of Silicon-Target and-Silicon-Carbon Negative Materials Engineering Technology, North Minzu University

Haojie Xu
Ningxia Research Center of Silicon-Target and-Silicon-Carbon Negative Materials Engineering Technology, North Minzu University

Kaiyi Chang
Ningxia Research Center of Silicon-Target and-Silicon-Carbon Negative Materials Engineering Technology, North Minzu University

Li Zhang
Ningxia Research Center of Silicon-Target and-Silicon-Carbon Negative Materials Engineering Technology, North Minzu University

Chang Li
Ningxia Research Center of Silicon-Target and-Silicon-Carbon Negative Materials Engineering Technology, North Minzu University

Jiao Hou
BOLT New Materials (Yinchuan) Co., Ltd

Xinwei Wang
BOLT New Materials (Yinchuan) Co., Ltd

Chunping Hou
houcp@nmu.edu.cn

Ningxia Research Center of Silicon-Target and-Silicon-Carbon Negative Materials Engineering Technology, North Minzu University

---

Research Article

Keywords: Silicon-based anode, N-doped carbon coating, Interfacial engineering, Lithium-ion batteries

Posted Date: May 22nd, 2026

DOI: https://doi.org/10.21203/rs.3.rs-9472287/v1

License: This work is licensed under a Creative Commons Attribution 4.0 International License.
Read Full License

Additional Declarations: No competing interests reported.

Version of Record: A version of this preprint was published at Journal of Materials Science: Materials in Electronics on August 11th, 2026. See the published version at https://doi.org/10.1007/s10854-026-18215-7.

Interfacial Engineering of Si@SiO_x with an N-Doped Carbon Shell for High-Performance Lithium-Ion Battery Anodes

Bowen Li[a], Haidong Xie[b], Hui Tian[a], Haojie Xu[a], Kaiyi Chang[a], Li Zhang[a], Chang Li[a], Jiao Hou[c], Xinwei Wang[c], Chunping Hou[a,c,d]*

[a] School of Materials Science and Engineering, Ningxia Research Center of Silicon-Target and-Silicon-Carbon Negative Materials Engineering Technology, North Minzu University, Yinchuan, 750021,China

[b] College of Chemical Engineering, Fuzhou University, Fuzhou, 350108, P. R. China

[c] Bolt New Material (Yinchuan) Co., Ltd, Yinchuan, 750002, P. R. China

[d] Institute of New-Energy Materials, Helanshan Laboratory, Yinchuan, 750021, P. R. China

*Correspondence author: houcp@nmu.edu.cn (Chunping Hou)

Abstract

With the increasing demand for high-energy-density lithium-ion batteries (LIBs), silicon-based anodes have attracted extensive attention because of their ultrahigh theoretical capacity and low lithiation potential. However, their practical application is still severely restricted by drastic volume variation during cycling and sluggish interfacial/electronic transport. In this work, a hierarchical Si@SiO_x@NC composite was successfully fabricated via in situ polymerization of a melamine-assisted resorcinol-formaldehyde resin on a preformed Si@SiO_x precursor, followed by carbonization under an inert atmosphere. The resulting composite features a core-shell structure composed of a crystalline Si core, an intermediate SiO_x layer, and an outer N-doped carbon shell. Structural characterizations demonstrate that the introduction of the nitrogen-containing resin precursor leads to the formation of a continuous amorphous outer shell with higher carbon content, larger specific surface area, and more developed small-mesopore characteristics than those of the Si@SiO_x@C counterpart. Benefiting from the synergistic effects of the SiO_x interlayer and the outer N-doped carbon shell, the optimized Si@SiO_x@NC electrode delivers a reversible capacity of 1022.3 $mAh \cdot g^{-1}$ after 200 cycles at 0.5 $A \cdot g^{-1}$ and 938 $mAh \cdot g^{-1}$ after 200 cycles at 1 $A \cdot g^{-1}$, together with a high initial coulombic efficiency of 74.08% and a reversible capacity of 1245 $mAh \cdot g^{-1}$ at 3 $A \cdot g^{-1}$. Kinetic analyses based on CV, GITT, EIS, and operando EIS/DRT measurements reveal that the N-doped carbon layer is associated with reduced charge-transfer resistance, improved Li^+ transport, and mitigated polarization fluctuation during dynamic cycling. These results suggest that constructing an outer N-doped carbon shell

on Si@SiO_x is a promising strategy for simultaneously enhancing the cycling stability and rate capability of silicon-based anodes.

Keywords: Silicon-based anode; N-doped carbon coating; Interfacial engineering; Lithium-ion batteries;

1 Introduction

With the growing demand for high-energy-density lithium-ion batteries, the development of advanced anode materials beyond commercial graphite has become an important research focus. Among the various candidates, silicon has been widely regarded as one of the most promising alternatives because of its ultrahigh theoretical specific capacity of up to 4200 $mAh \cdot g^{-1}$, low working potential, and natural abundance[1-3]. However, the practical application of Si anodes is still severely hindered by two major issues, namely poor intrinsic electronic conductivity and drastic volume variation during repeated lithiation/delithiation. The huge volume expansion of silicon, which can exceed 300%, usually leads to particle pulverization, electrode structural disintegration, and repeated rupture/reconstruction of the solid electrolyte interphase (SEI), thereby resulting in rapid capacity decay, low coulombic efficiency, and poor long-term cycling stability[4-6]. These drawbacks have greatly limited the practical application of silicon-based anodes in high-energy-density lithium-ion batteries.

To address these issues, extensive efforts have been devoted to the structural and interfacial engineering of Si-based anodes, including nanosizing, porous structure design, alloying, surface oxidation, and carbon compositing[7]. Among these strategies, carbon coating is considered one of the most mature and effective approaches. A conformal carbon layer can serve as an elastic buffer to alleviate the mechanical stress induced by volume fluctuation, while simultaneously improving electrical conductivity and facilitating electron/Li^+ transport. In addition, the carbon shell can partially isolate the Si surface from direct contact with the electrolyte, suppress

excessive side reactions, and mitigate repeated SEI rupture and reformation, thus improving interfacial stability and cycling durability. In particular, carbon materials with high elasticity or porous characteristics have shown considerable advantages in reducing interfacial polarization and accommodating cyclic stress[8-11]. Furthermore, heteroatom doping, especially nitrogen doping, can effectively tailor the electronic structure of carbon, introduce abundant defect and polar sites, and accelerate charge-transfer kinetics, thereby further enhancing the electrochemical performance of Si-based electrodes[12, 13].

Besides carbon modification, surface oxidation of silicon has also attracted considerable attention in recent years. The introduction of a SiO_x layer on the Si surface can provide a relatively rigid protective framework, alleviate local stress concentration during cycling, and enhance interfacial stability[14]. More importantly, SiO_x can undergo partial irreversible conversion during the initial lithiation process to generate buffering phases such as lithium silicates and Li_2O, which help accommodate volume change and maintain structural integrity[15]. Therefore, the rational integration of SiO_x and carbon layers is expected to combine the advantages of rigid mechanical buffering and flexible conductive protection. In particular, hierarchical core-shell or multilayer structures have demonstrated great potential for simultaneously regulating electron transport, Li^+ diffusion, and electrode/electrolyte interfacial stability[16, 17]. However, although many previous studies have focused on single carbon coating, SiO_x protection, or binary $Si/SiO_x/C$ composites, the synergistic design of multifunctional triple-layer architectures with distinct mechanical, conductive, and interfacial

roles remains insufficiently explored.

Inspired by these considerations, a hierarchical Si@SiO_x@NC architecture is proposed in this work for high-performance lithium-ion battery anodes. In this design, a SiO_x interlayer is first constructed on the Si surface through VTMS-assisted hydrolysis and condensation to enhance structural robustness and interfacial stability. Subsequently, a nitrogen-containing resin layer is formed on the Si@SiO_x surface via in situ polymerization under alkaline conditions and is then converted into an outer N-doped carbon shell after thermal treatment. Through the synergistic integration of the Si core, the SiO_x interlayer, and the outer N-doped carbon shell, the as-designed structure is expected to alleviate volume expansion, stabilize the interfacial environment, and facilitate charge-transfer and ion-transport processes, thereby contributing to enhanced specific capacity, cycling stability, and rate capability. This work provides a rational interfacial design strategy for the development of advanced silicon-based anodes toward high-energy-density lithium-ion batteries.

2. Experimental section

2.1 Materials

Silicon (Si) was obtained from Bolt New Materials (Yinchuan) Co., Ltd. Vinyl trimethoxy silane (VTMS), cetyltrimethylammonium bromide (CTAB), resorcinol, formaldehyde, ammonia solution, and melamine were purchased from Shanghai Macklin Biochemical Technology Co., Ltd. For electrode preparation and electrochemical evaluation, poly(acrylic acid) (PAA, average Mv ≈ 100,000) was purchased from Wengjiang Chemical Reagent Co., Ltd., and Super P

conductive carbon was supplied by Guangdong Canrd New Energy Technology Co., Ltd. Celgard 2400 membranes were used as separators. Lithium metal foils and the electrolyte were obtained from Jiaxing Naxin New Material Technology Co., Ltd. Unless otherwise specified, all reagents used in this work were of analytical grade.

2.2 Preparation of Si@SiO_x Composite

The Si@SiO_x composite was synthesized via a surfactant-assisted silane hydrolysis-condensation strategy. In a typical synthesis, 0.5 g of Si powder was dispersed in 100 mL of deionized water under continuous magnetic stirring and ultrasonication. Subsequently, 1.0 g of CTAB was introduced as a surfactant to improve the dispersion uniformity of the Si particles. Thereafter, VTMS was added to the suspension, and the reaction mixture was maintained under stirring at room temperature for 10 h, during which hydrolysis and condensation of VTMS occurred to form a SiO_x coating layer on the Si surface. After the reaction, the obtained product was collected by vacuum filtration and dried at 100 ℃ to yield the Si@SiO_x composite.

2.3 Preparation of Si@SiO_x@NC Composite

Si@SiO_x@NC was synthesized via an in situ polymerization-carbonization route. Typically, 0.5 g of Si@SiO_x was dispersed in 100 mL of 50 vol% aqueous ethanol under magnetic stirring for 2 h, followed by ultrasonication for 1 h. Subsequently, 0.125 mL of aqueous ammonia, 0.25 g of resorcinol, 1.0 g of melamine, and 0.27 mL of formaldehyde were sequentially introduced into the suspension, with an additional stirring interval of 30 min after the addition of ammonia and resorcinol, respectively. The mixture was then stirred continuously for 24 h to form a nitrogen-

containing polymer coating on the Si@SiO_x surface. After centrifugation at 8000 r·min^{-1} and vacuum drying at 80 ℃ for 12 h, the obtained precursor was calcined at 700 ℃ for 3 h under an Ar atmosphere to yield the Si@SiO_x@NC composite.

For comparison, a control sample was prepared under the identical conditions except that melamine was not added during the synthesis process. The resulting undoped composite was denoted as Si@SiO_x@C.

2.4 Structural characterization

The morphology of the samples was first characterized by scanning electron microscopy (SEM, SIGMA 500), and their internal microstructure was further examined by transmission electron microscopy (TEM, JEM-2100). The phase composition of the samples was identified by X-ray diffraction (XRD-6000) using Cu Kα radiation. Fourier transform infrared (FTIR) spectra were recorded on a Nicolet iS50 spectrometer to analyze the surface functional groups. Thermogravimetric analysis (TGA) was carried out on an STA 449 F3 thermal analyzer in air from room temperature to 800 ℃ at a heating rate of 10 ℃ min^{-1}. The textural properties, including the Brunauer-Emmett-Teller (BET) specific surface area and pore-size distribution, were determined from N_2 adsorption-desorption measurements using a 3H-2000 PM1 analyzer. Raman spectra were collected on a Horiba LabRAM HR Evolution spectrometer. The surface elemental composition and chemical states were analyzed by X-ray photoelectron spectroscopy (XPS) on an ESCALAB Xi+ instrument.

3. Results and discussion

3.1 Morphological and structural characterization of the Si-based composites

Fig. 1 schematically illustrates the synthesis procedure and structural evolution of the Si@SiO_x@NC composite. Using the preformed Si@SiO_x precursor as the starting material, resorcinol, formaldehyde, and melamine were in situ co-polymerized on the particle surface under weakly alkaline conditions to generate a uniform organic resin coating. After subsequent calcination under an inert atmosphere, the outer resin layer was carbonized into an N-doped amorphous carbon shell, thereby yielding the Si@SiO_x@NC composite. The resulting hierarchical core-shell architecture, consisting of a Si core, an intermediate SiO_x layer, and an outer NC shell, is expected to synergistically improve structural stability and interfacial kinetics. In this configuration, the Si core serves as the main capacity-contributing component, the SiO_x interlayer helps buffer volume variation and reinforce interfacial stability, and the outer continuous N-doped carbon shell enhances electronic transport, suppresses direct contact between active particles and the electrolyte, and may help regulate interfacial reactions through its defect-rich and polar surface characteristics. As a result, such a rationally designed structure is expected to be favorable for improving the cycling stability and rate capability of the Si-based anode.

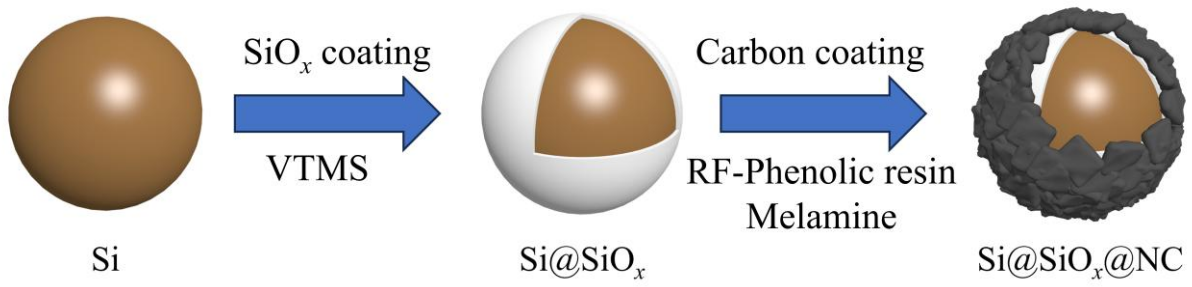


Fig. 1. Schematic illustration of the synthesis process for Si@SiO_x@NC composites

The morphological evolution of Si, Si@SiO_x, Si@SiO_x@C, and Si@SiO_x@NC was systematically examined by scanning electron microscopy (SEM), as shown in Fig. 2. As presented in Fig. 2(a), the pristine Si nanoparticles exhibit a nearly spherical morphology with a relatively concentrated particle-size distribution, although a certain degree of agglomeration is already observed due to the high surface energy of nanosized Si particles. After VTMS-assisted hydrolysis and condensation, the morphology of Si@SiO_x changes noticeably, as shown in Fig. 2(b). Compared with pristine Si, the particles become larger overall, the interparticle connections become tighter, and the boundaries between individual particles become less distinct, indicating that the introduction of the SiO_x coating layer has significantly altered the particle surface characteristics. After subsequent resin coating and carbonization, the SEM images of Si@SiO_x@C and Si@SiO_x@NC are shown in Fig. 2(c, d), respectively. Both samples no longer appear as well-dispersed individual nanoparticles, but instead evolve into micron-sized secondary agglomerates assembled from numerous smaller primary particles, revealing an evident hierarchical structural feature. Compared with Si@SiO_x@C, Si@SiO_x@NC exhibits a rougher and looser surface texture with more pronounced undulations, while the boundaries between the original nanoparticles become further obscured. This suggests that the introduction of the nitrogen-containing resin precursor leads to a more substantial surface reconstruction during the formation of the outer carbon shell. Overall, these results indicate that the subsequent coating and carbonization processes not only modify the surface morphology of the particles, but

also promote the evolution of primary nanoparticles into hierarchical secondary structures. Such structural characteristics are generally favorable for constructing a continuous outer coating network and providing more accessible surface area for electrolyte infiltration and interfacial contact, which may be beneficial for subsequent electrochemical reactions[18].

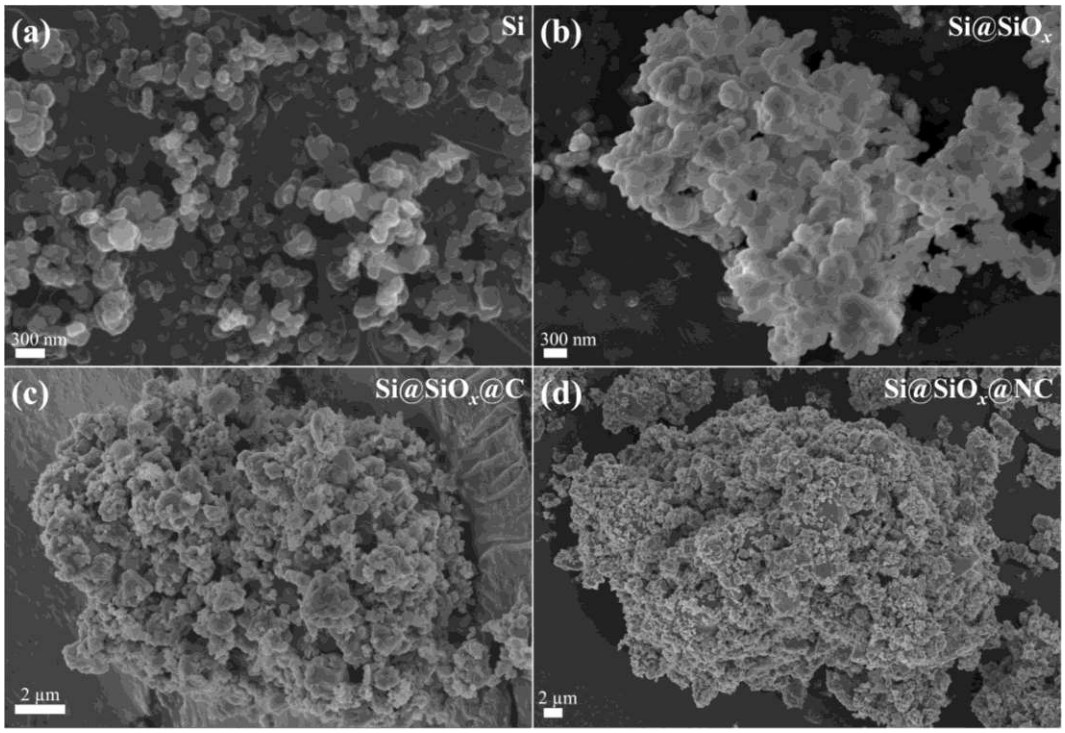


Fig. 2. (a) SEM image of Si, (b) SEM image of Si@SiO_x, (c) SEM image of Si@SiO_x@C, (d) SEM image of Si@SiO_x@NC

The internal structure of Si@SiO_x@NC was further investigated by TEM and EDS analyses, as shown in Fig. 3. The low-magnification TEM images in Fig. 3(a, d) reveal that the composite is composed of aggregated nanoparticles, with a discernible and continuous outer coating layer surrounding the particle assembly. As shown in the HRTEM images in Fig. 3(b, c), clear lattice fringes can be observed in the inner crystalline domains, with measured interplanar spacings of

0.3162 and 0.3129 nm, which can be assigned to the (111) plane of crystalline Si[19]. Outside the crystalline region, an amorphous coating layer with a thickness of approximately 13 nm is clearly observed, which can be reasonably attributed to the composite outer shell formed by SiO_x and N-doped carbon. Furthermore, the EDS elemental mapping images demonstrate that Si, O, C, and N are all distributed throughout the particle region, while the spatial distributions of C and N closely follow the particle contours, confirming that the nitrogen-containing carbon component is predominantly located in the outer layer of the composite[20]. In combination with the SEM observations in Fig. 2, these results indicate that the micron-sized agglomerates are essentially hierarchical composite structures consisting of crystalline Si nanodomains and an amorphous SiO_x/NC outer layer.

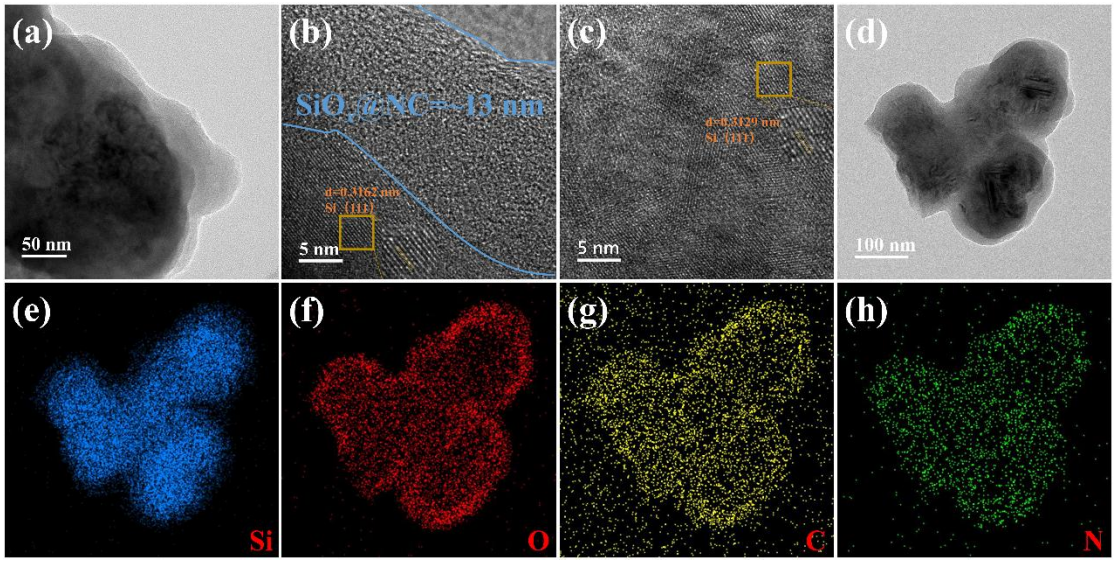


Fig. 3. TEM images and EDS elemental distribution maps of Si@SiO_x@NC

The XRD patterns of Si@SiO_x@C and Si@SiO_x@NC are presented in Fig. 4(a). Both samples exhibit distinct diffraction peaks at approximately 28.4°, 47.3°, 56.1°, 69.1°, and 76.4°,

which can be well indexed to crystalline Si, indicating that the crystalline framework of Si is well preserved after carbon coating and the introduction of the nitrogen-containing carbon precursor. In addition, the two samples show highly similar diffraction features, and no obvious new impurity peaks are detected, suggesting that the subsequent coating process does not alter the crystal structure of the Si core. Considering the composition of the composites, the surface SiO_x layer and the outer carbon shell are likely amorphous in nature and therefore do not give rise to distinct sharp diffraction signals in the XRD patterns[21].

The FTIR spectra of the two samples are shown in Fig. 4(b) to further probe their surface chemical structures. A broad absorption band centered around 3400 cm^{-1} is observed for both samples, which is generally associated with O-H stretching vibrations from surface hydroxyl groups or adsorbed water. In the range of 1050-1100 cm^{-1}, both samples display a strong absorption band that can be assigned to the stretching vibration of Si-O-Si bonds, indicating the presence of relatively stable silicon-oxygen species on the surface. In addition, absorption features in the lower-wavenumber region can be related to Si-O-C bonds, implying interfacial interaction between the carbon layer and the SiO_x component[22]. Compared with Si@SiO_x@C, Si@SiO_x@NC shows a slight difference in the spectral feature near 1600 cm^{-1}, which may be associated with the altered surface chemical environment after the introduction of the N-doped carbon layer, although contributions from O-H-related vibrations in this region cannot be excluded[23].

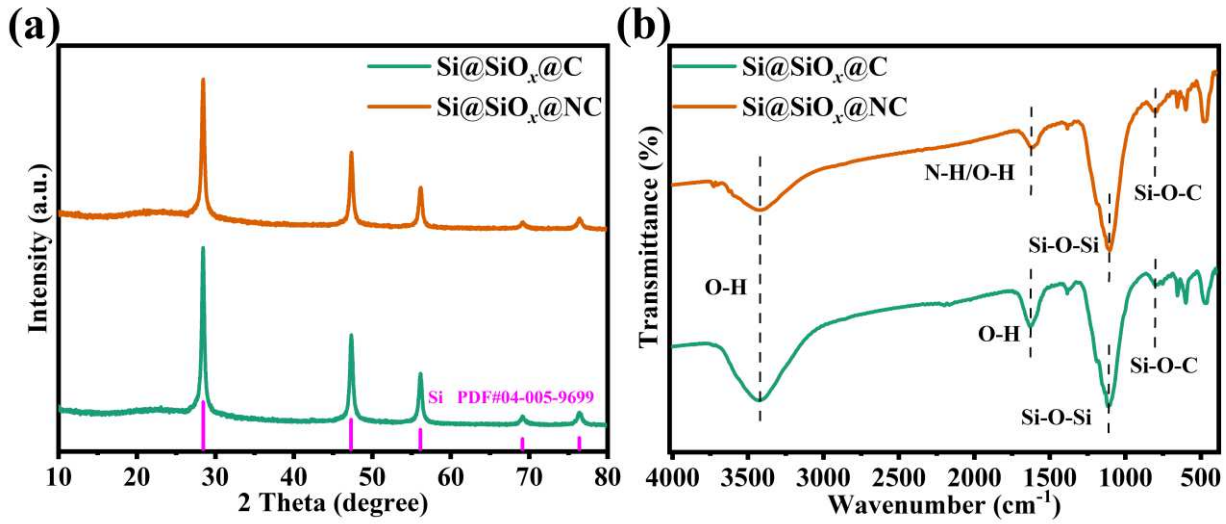


Fig. 4. (a) XRD patterns and (b) FTIR spectra of Si@SiO$_x$@C and Si@SiO$_x$@NC

As shown in Fig. 5(a-c), the two composites exhibit evident differences in thermal behavior and pore structure. The TGA curves in Fig. 5(a) show that, after heating to 700 °C in air, the residual masses of Si@SiO$_x$@C and Si@SiO$_x$@NC are 86.7% and 82.5%, respectively. Accordingly, the apparent carbon-related weight losses are estimated to be about 13.3 wt% for Si@SiO$_x$@C and 17.5 wt% for Si@SiO$_x$@NC, indicating a higher carbonaceous content in the N-doped sample. The N_2 adsorption-desorption isotherms in Fig. 5(b) further reveal that both Si@SiO$_x$@C and Si@SiO$_x$@NC exhibit markedly increased adsorption capacities compared with the Si@SiO$_x$ precursor, suggesting that the coating process plays an important role in the development of the pore structure. Notably, Si@SiO$_x$@NC shows a higher overall adsorption uptake than Si@SiO$_x$@C, especially in the high-relative-pressure region, implying a more developed porous texture and a larger pore volume. This tendency is well supported by the quantitative data: the BET specific surface area increases from 16.58 $m^2 \cdot g^{-1}$ for Si@SiO$_x$@C to

67.49 $m^2 \cdot g^{-1}$ for Si@SiO_x@NC, while the total pore volume correspondingly rises from 0.0536 to 0.0733 $cm^3 \cdot g^{-1}$. In addition, the pore-size distribution curves in Fig. 5(c) show that Si@SiO_x@NC possesses a smaller BJH adsorption average pore size of 8.25 nm, compared with 13.35 nm for Si@SiO_x@C. Meanwhile, the dV/dD profiles indicate that Si@SiO_x@NC contributes a larger pore volume in the 2-5 nm range. These results suggest that the introduction of melamine not only increases the carbon-related fraction in the composite, but also promotes the formation of a more developed porous structure with higher specific surface area and more pronounced small-mesopore characteristics[24].

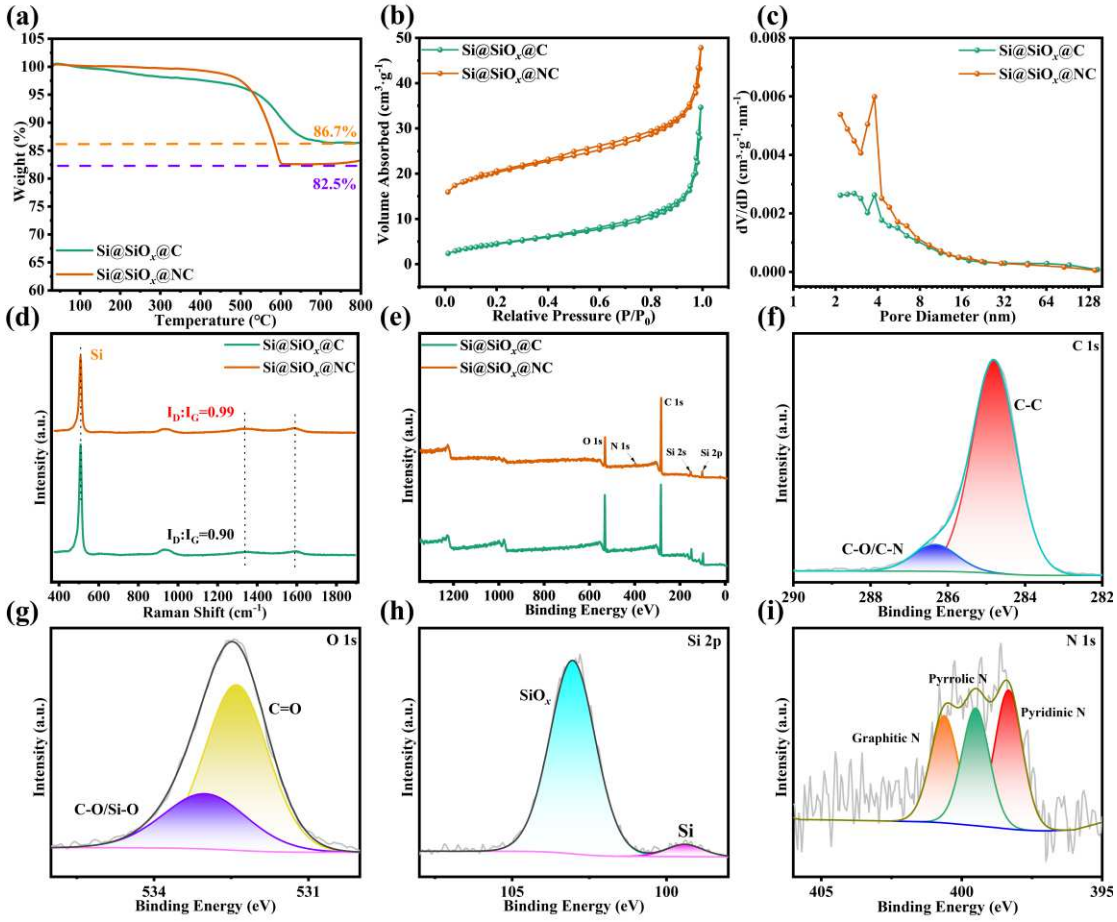


Fig. 5. (a) TG curves, (b) N_2 adsorption-desorption isotherms, (c) pore size distribution curves, (d)

Raman spectra, and (e) XPS survey spectra of Si@SiO_x@C and Si@SiO_x@NC, and high-resolution (f) C 1s, (g) O 1s, (h) Si 2p, and (i) N 1s spectra of Si@SiO_x@NC

The Raman and XPS results of the samples are presented in Fig. 5(d-i). In the Raman spectra, besides the characteristic peak of crystalline Si at around 520 cm^{-1}, both samples exhibit the typical D band and G band at approximately 1350 and 1590 cm^{-1}, respectively. It should be noted that the I_D/I_G values reported here were calculated from the maximum intensities of the D and G bands. Based on this method, the I_D/I_G ratios of Si@SiO_x@C and Si@SiO_x@NC are 0.90 and 0.99, respectively, indicating that the introduction of nitrogen increases the degree of structural disorder and the density of defect sites in the carbon layer[25].Consistent with the Raman analysis, XPS further reveals the surface elemental composition and chemical states of the outer shell. In the survey spectrum, Si@SiO_x@NC shows distinct C 1s, O 1s, N 1s, Si 2s, and Si 2p signals, whereas no N 1s signal is detected for Si@SiO_x@C, confirming that the nitrogen-containing carbon precursor effectively alters the surface elemental composition of the composite. The high-resolution spectra show that the C 1s signal can be mainly deconvoluted into C-C and C-O/C-N components, while the O 1s spectrum is primarily composed of C-O/Si-O and C=O species. The Si 2p spectrum is dominated by SiO_x-related species, accompanied by only a weak Si^0 contribution, which is consistent with the surface-sensitive nature of XPS and the existence of a SiO_x/carbon coating layer on the particle surface. In addition, the N 1s spectrum can be deconvoluted into pyridinic N, pyrrolic N, and graphitic N, demonstrating that nitrogen has been successfully incorporated into the surface carbon network[26, 27].

3.2 Electrochemical performances of Si@SiO_x@NC

To compare the lithium-storage behavior of Si@SiO_x@C and Si@SiO_x@NC, their cycling stability and initial galvanostatic charge-discharge characteristics were systematically evaluated, as shown in Fig. 6(a-d). Figures 6(a) and 6(b) present the cycling performances of the two composites at 0.5 and 1 $A \cdot g^{-1}$, respectively, after an initial activation process of five cycles at 0.1 $A \cdot g^{-1}$. With prolonged cycling, Si@SiO_x@NC exhibits a much slower capacity decay than Si@SiO_x@C. After 200 cycles at 0.5 $A \cdot g^{-1}$, Si@SiO_x@NC still maintains a reversible specific capacity of about 1022.3 $mAh \cdot g^{-1}$, whereas Si@SiO_x@C retains only 675.1 $mAh \cdot g^{-1}$. A similar trend is observed at 1 $A \cdot g^{-1}$, where Si@SiO_x@NC delivers 938 $mAh \cdot g^{-1}$ after 200 cycles, which is distinctly higher than that of Si@SiO_x@C (608 $mAh \cdot g^{-1}$). These results indicate that Si@SiO_x@NC exhibits better cycling stability than Si@SiO_x@C under prolonged cycling at relatively high current densities.

The initial galvanostatic charge-discharge profiles of the two samples at 0.1 $A \cdot g^{-1}$ are shown in Fig. 6(c, d). Both electrodes exhibit an obvious low-voltage plateau during the first discharge process, which is generally associated with interfacial film formation and related electrochemical reactions during the initial activation cycle. From the second cycle onward, the charge-discharge curves largely overlap, indicating good reversibility after the initial activation. Notably, Si@SiO_x@NC exhibits a higher initial coulombic efficiency (ICE) of 74.08%, with first-cycle discharge/charge capacities of 3374.5/2499.8 $mAh \cdot g^{-1}$, compared with 67.76% for Si@SiO_x@C (3722.4/2522.3 $mAh \cdot g^{-1}$). The higher ICE indicates relatively lower irreversible lithium

consumption during the initial cycle for Si@SiO$_x$@NC. This result suggests that the introduction of the nitrogen-containing resin-derived carbon layer may help suppress side reactions in the first cycle and improve the initial reversibility of the electrode, thereby contributing to more favorable interfacial conditions for subsequent stable cycling[28].

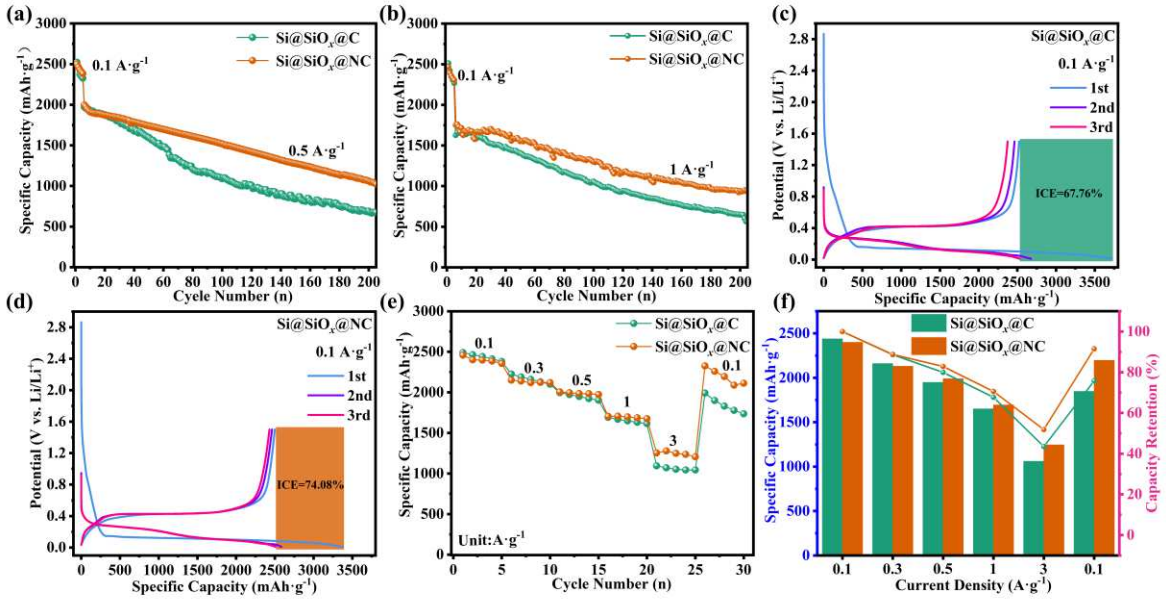


Fig. 6. (a) Cycling performance at 0.5 A·g^{-1}, (b) cycling performance at 1 A·g^{-1}, (c) initial three charge/discharge curves of Si@SiO$_x$@C, (d) initial three charge/discharge curves of Si@SiO$_x$@NC, (e) rate performance, and (f) capacity retention at different current densities of Si@SiO$_x$@C and Si@SiO$_x$@NC

The rate performances of Si@SiO$_x$@C and Si@SiO$_x$@NC at different current densities are further compared in Fig. 6(e, f). As the current density increases stepwise from 0.1, 0.3, 0.5, and 1 A·g^{-1} to 3 A·g^{-1}, the average specific capacities of Si@SiO$_x$@C are 2438, 2160, 1949, 1651, and 1061 mAh·g^{-1}, respectively, whereas those of Si@SiO$_x$@NC are 2400, 2130,

1989, 1694, and 1245 $mAh \cdot g^{-1}$, respectively. Overall, the two samples exhibit comparable capacities at relatively low current densities, whereas the advantage of Si@SiO_x@NC becomes increasingly evident at 0.5 $A \cdot g^{-1}$ and above. In particular, at 3 $A \cdot g^{-1}$, Si@SiO_x@NC still delivers a reversible specific capacity of about 1245 $mAh \cdot g^{-1}$, which is clearly higher than that of Si@SiO_x@C (1061 $mAh \cdot g^{-1}$). When the current density is switched back to a lower value, Si@SiO_x@NC recovers an average capacity of 2196 $mAh \cdot g^{-1}$, whereas Si@SiO_x@C recovers only about 1847 $mAh \cdot g^{-1}$, indicating the better electrochemical reversibility of the former. These results demonstrate that the introduction of the nitrogen-containing resin-derived carbon layer is beneficial for improving the rate capability of the composite under high-current conditions. Such enhancement can be reasonably attributed to the more continuous electron-transport pathway provided by the outer carbon shell, together with the defect-rich and polar features introduced by N doping, which may facilitate interfacial reaction kinetics and ion transport, thereby enabling the superior high-rate performance of Si@SiO_x@NC[29]. For contextual comparison, the cycling and rate performances of the Si@SiO_x@NC electrode were compared with those of recently reported Si-based composites over the past three years, as summarized in Table 1.

Table 1 Comparison of the cycling and rate performances of the Si@SiO_x@NC prepared in this work with other recently reported Si-based composites over the past three years.

Sample	Cycling performance ($mAh \cdot g^{-1}$)	Rate capability ($mAh \cdot g^{-1}$)	Year	Ref.
Si@SiO_x@NC	1022.3 (after 200 cycles at 0.5 $A \cdot g^{-1}$)	1245 (3.0 $A \cdot g^{-1}$)	/	This work
Si-SiO_x/C-1.25	630 (after 250 cycles at 0.2 $A \cdot g^{-1}$)	452 (1.5 $A \cdot g^{-1}$)	2025	[30]
Si/CNTs-2	922.4 (after 200 cycles at 0.2$A \cdot g^{-1}$)	836 (2.0 $A \cdot g^{-1}$)	2024	[31]

Si@GC/PAC	600 (after 200 cycles at 0.1 A·g^{-1})	797 (5.0 A·g^{-1}) 603 (2.0 A·g^{-1}) 503 (5.0 A·g^{-1})	2023	[32]
Si/Gt/RGO	1007.0 (after 100 cycles at 0.2 A·g^{-1})	475.8 (3.0 A·g^{-1})	2023	[33]
RNC@Si-50%	589 (after 100 cycles at 0.1 A·g^{-1})	340.0 (0.5 A·g^{-1})	2025	[19]

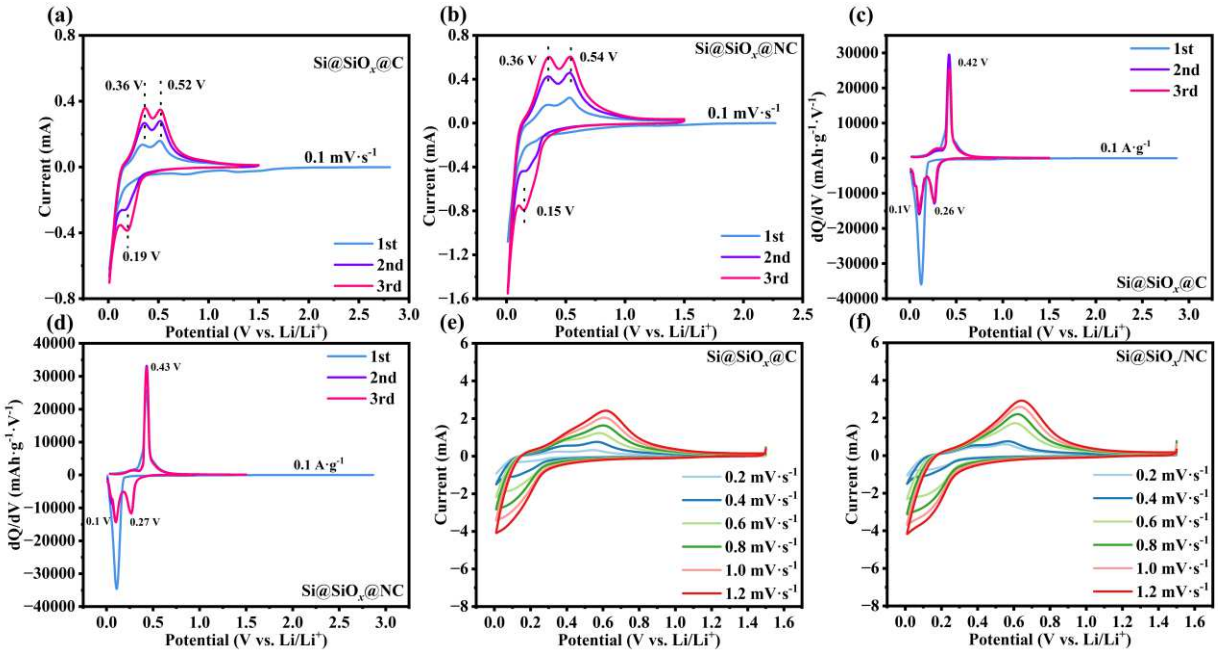


Fig. 7. CV curves at a scan rate of 0.1 mV·s^{-1}: (a) Si@SiO$_x$@C, (b) Si@SiO$_x$@NC; The dQ/dV curves of (c) Si@SiO$_x$@C, (d) Si@SiO$_x$@NC at 0.1 A·g^{-1}; CV curves at scan rates from 0.2 mV·s^{-1} to 1.2 mV·s^{-1}: (e) Si@SiO$_x$@C, (f) Si@SiO$_x$@NC

As shown in Fig. 7(a, b), both Si@SiO$_x$@C and Si@SiO$_x$@NC electrodes exhibit pronounced first-cycle activation features in the initial three CV curves. During the first cathodic scan, a broad and intense reduction response appears in the low-potential region for both electrodes, which is generally associated with electrolyte decomposition on the electrode surface, the initial formation of the SEI layer, and the partially irreversible conversion of SiO$_x$ in the first cycle[34]. In the second and third cycles, this broad cathodic feature becomes markedly weakened, while the corresponding anodic peaks gradually become well defined, appearing at

around 0.36/0.52 V for Si@SiO_x@C and 0.36/0.54 V for Si@SiO_x@NC. Moreover, the substantial overlap between the latter two cycles indicates that both electrodes gradually evolve into a relatively stable and reversible lithiation/delithiation process after the initial activation.

The dQ/dV curves in Fig. 7(c, d) further reveal the differences in the reaction behavior of the two samples. Both electrodes exhibit a distinct anodic peak at about 0.42-0.43 V, together with several cathodic features in the low-potential region, including responses around 0.1 V and 0.26/0.27 V, which are commonly associated with the alloying/dealloying reactions of the Li-Si system during lithiation and delithiation. Compared with Si@SiO_x@C, Si@SiO_x@NC shows sharper and more intense peaks, whereas the peaks of Si@SiO_x@C are relatively broader. This difference suggests that Si@SiO_x@NC may undergo lower polarization and more favorable reaction kinetics during cycling. Although such behavior cannot be interpreted solely from individual peak features, it is well consistent with the trends observed in the cycling and rate-performance results. As shown in Fig. 7(e, f), when the scan rate increases from 0.2 to 1.2 $mV \cdot s^{-1}$, the redox peak currents of both electrodes increase accordingly, accompanied by only limited peak shifts, indicating that both electrodes can maintain electrochemical responsiveness over a relatively wide scan-rate range. Meanwhile, Si@SiO_x@NC consistently exhibits higher current responses than Si@SiO_x@C at all scan rates, and this difference becomes more pronounced at higher scan rates. This result indicates that the introduction of the N-doped carbon layer is beneficial for maintaining relatively efficient electron/ion transport under fast reaction conditions. Taken together, the CV and dQ/dV results suggest that the outer N-doped carbon layer modifies

the interfacial environment of the particles and may improve the reaction kinetics of the electrode to a certain extent, which is consistent with its superior cycling and rate performances[35].

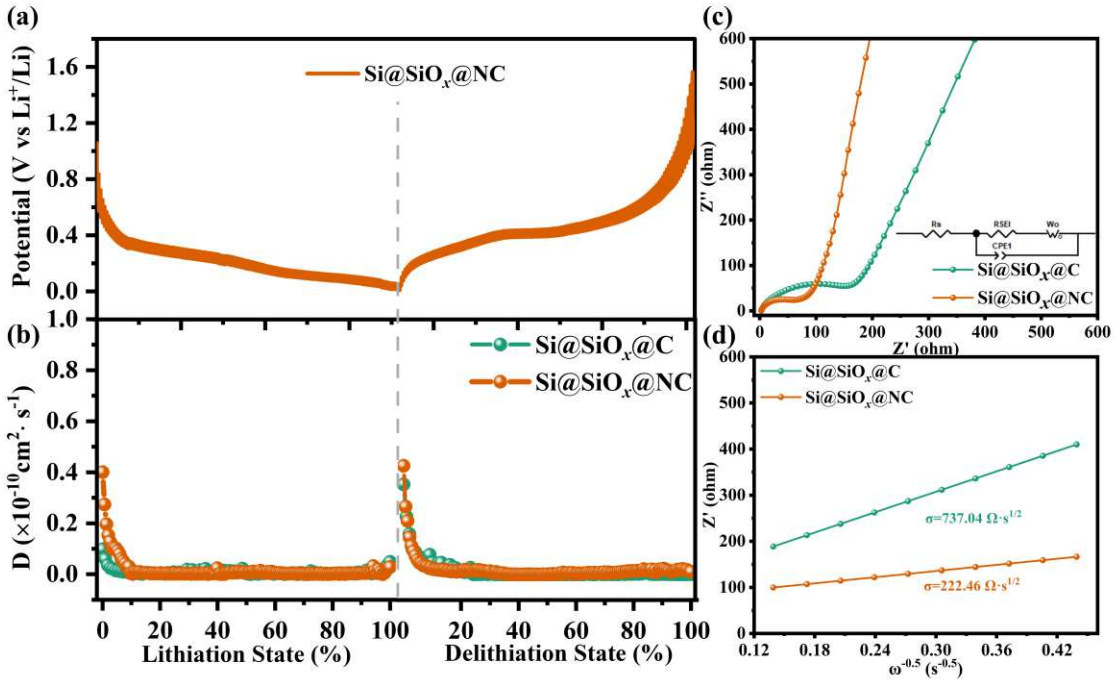


Fig. 8. (a) GITT curve of Si@SiO$_x$@NC at 0.5 A·g^{-1}; (b) D_{Li^+}, (c) pre-cycling EIS curves, and (d) linear fitting curves in the low-frequency region of the impedance spectra for Si@SiO$_x$@C and Si@SiO$_x$@NC

To further elucidate the Li^+ transport kinetics of the silicon-based composite anodes, galvanostatic intermittent titration technique (GITT) measurements were carried out, as shown in Fig. 8(a). Assuming that Li^+ diffusion in the active material follows Fick's second law, the apparent Li^+ diffusion coefficient $(D_{Li^+})$was calculated according to[36]:

$$D_{Li^+}=\frac{4}{\pi\tau}\left(\frac{m_B V_m}{A M_B}\right)^2\left(\frac{\Delta E_s}{\Delta E_t}\right)^2 \quad (1)$$

where τ is the duration of the current pulse, m_B is the mass of the active material, V_m is the molar volume, A is the electrode contact area, M_B is the molar mass of the active material, ΔE_s is

the steady-state voltage change, and ΔE_t is the total voltage change during the current pulse.

As shown in Fig. 8(b), the apparent Li^+ diffusion coefficient exhibits a pronounced dependence on the lithiation/delithiation state. For the Si@SiO_x@NC electrode, the D_{Li^+} values range from 1.35×10^{-15} to 4×10^{-11} $cm^2\cdot s^{-1}$ during lithiation and from 2.57×10^{-15} to 4.26×10^{-11} $cm^2\cdot s^{-1}$ during delithiation. In comparison, the Si@SiO_x@C electrode shows overall lower diffusion coefficients, with values ranging from 2.42×10^{-15} to 9.8×10^{-12} $cm^2\cdot s^{-1}$ during lithiation and from 1.41×10^{-15} to 3.53×10^{-11} $cm^2\cdot s^{-1}$ during delithiation. In general, both electrodes maintain relatively high D_{Li^+} values at the initial stage of lithiation/delithiation, followed by a rapid decrease and then a relatively low level over the intermediate reaction region. Notably, Si@SiO_x@NC exhibits consistently higher apparent Li^+ diffusion coefficients than Si@SiO_x@C during both lithiation and delithiation, indicating that N-doping is favorable for enhancing Li^+ transport kinetics in the composite electrode.

Electrochemical impedance spectroscopy (EIS) results further confirm the kinetic advantage of the Si@SiO_x@NC electrode, as shown in Fig. 8(c). The Nyquist plots consist of a depressed semicircle in the high-to-medium frequency region and an inclined line in the low-frequency region, corresponding to the interfacial charge-transfer process and diffusion-related impedance, respectively[37]. The fitted results show that the charge-transfer resistance is significantly reduced from 133.28 Ω for the Si@SiO_x@C electrode to 50.72 Ω for the Si@SiO_x@NC electrode, indicating that N-doping effectively accelerates the interfacial charge-transfer kinetics.

In the Warburg region, the real part of the impedance Z' satisfies the following

relationship[38]:

$$Z' = R_s + R_{ct} + \sigma\omega^{-0.5} \quad (2)$$

Therefore, the Warburg coefficient (σ) can be extracted from the linear fitting of Z' versus $\omega^{-0.5}$, as shown in Fig. 8(d). The calculated σ values for Si@SiO_x@C and Si@SiO_x@NC are 737.04 and 222.46 $\Omega \cdot s^{-0.5}$, respectively. Under the approximation of the semi-infinite diffusion model, the apparent Li^+ diffusion coefficient can be further calculated according to:

$$D_{Li^+} = \frac{0.5R^2T^2}{A^2F^4C^2\sigma^2n^4} \quad (3)$$

Based on this calculation, the apparent Li^+ diffusion coefficients of Si@SiO_x@C and Si@SiO_x@NC are determined to be $5.11\times10^{-14}$and 5.60×10^{-13} $cm^2 \cdot s^{-1}$, respectively. Although the absolute D_{Li^+} values derived from GITT and EIS are inherently apparent and may be affected by differences in measurement principles and data-processing methods, both techniques consistently reveal the same variation trend, demonstrating that the Si@SiO_x@NC electrode possesses lower diffusion-related resistance and faster Li^+ transport kinetics. Combined with the GITT and EIS results, it can be inferred that the introduction of the N-doped carbon layer is beneficial for interfacial charge-transfer and ion/electron transport within the electrode, thereby helping reduce polarization and improve reaction reversibility. Meanwhile, the uniformly coated N-doped carbon layer is also expected to buffer volume variation and maintain structural integrity, which may help retard the accumulation of interfacial impedance during cycling. Therefore, the interfacial regulation effect induced by the N-doped carbon layer is considered to contribute to the enhanced electrochemical reaction kinetics of the silicon-based composite electrode, and thus

to its improved rate capability and cycling stability.

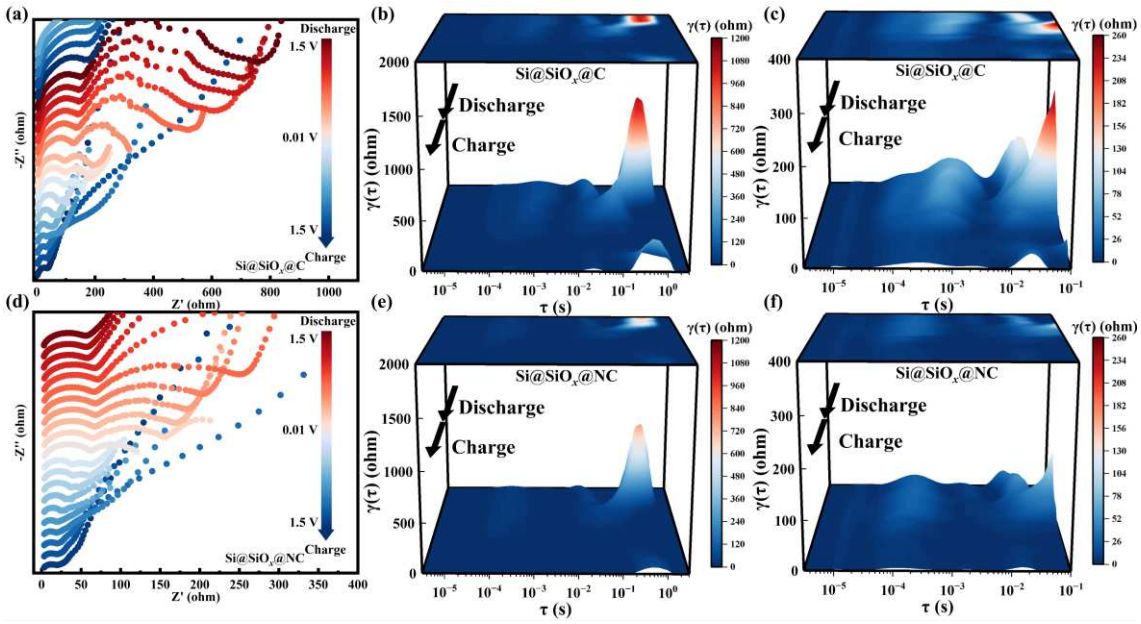


Fig. 9. Electrochemical characterizations of Si@SiO$_x$@C and Si@SiO$_x$@NC: (a, d) Nyquist plots evolving with voltage during the charge and discharge process (the color bar represents the battery voltage); (b, e) corresponding 3D DRT spectra with relaxation time as a variable; (c, f) 3D DRT spectra in the high-frequency region (short relaxation time)

To further investigate the impedance evolution of the electrodes during practical charge-discharge processes, operando electrochemical impedance spectroscopy measurements were performed on the Si@SiO$_x$@C and Si@SiO$_x$@NC electrodes, and the results are shown in Fig. 9(a, d). Throughout the full charge-discharge window (1.5 V-0.01 V-1.5 V), the Nyquist plots of both electrodes vary continuously with the change in potential, indicating that the interfacial reactions and Li^+ transport processes are dynamically adjusted during cycling rather than remaining constant[39]. Overall, the Si@SiO$_x$@NC electrode exhibits a lower impedance response over the entire voltage range, as evidenced by the generally smaller semicircles in the

high-to-medium frequency region and the less pronounced tail in the low-frequency region, suggesting lower charge-transfer resistance and diffusion-related impedance. In contrast, the Si@SiO_x@C electrode shows a larger variation in impedance, particularly in the medium- and low-frequency regions, implying that its interfacial processes are more sensitive to potential change and more susceptible to aggravated polarization and mass-transport limitations during cycling. The more moderate impedance evolution of Si@SiO_x@NC is also consistent with the above ex situ EIS results.

To further distinguish the impedance contributions of different electrochemical processes in the operando EIS spectra, the data were transformed into DRT profiles, as shown in Fig. 9(b, c, e, f). The Si@SiO_x@C electrode exhibits pronounced relaxation responses over a broad τ range, and these characteristic peaks vary markedly with the change in potential, not only in intensity but also, in some regions, in peak shape. This behavior suggests that the SEI-related process, charge-transfer process, and diffusion-related process undergo more substantial fluctuations during cycling[40, 41]. By comparison, Si@SiO_x@NC displays an overall weaker DRT response, with all characteristic peaks showing reduced intensity and relatively smaller variations throughout the whole charge-discharge process. This difference is particularly evident in the enlarged short-τ, indicating that the N-doped carbon layer may play a more pronounced role in regulating high-frequency interfacial processes.

Overall, the operando Nyquist and DRT analyses consistently indicate that the introduction of the N-doped carbon layer helps moderate the impedance evolution of the electrode throughout

the charge-discharge process. In addition to lowering the overall impedance level, the N-doped carbon shell also appears to mitigate the potential-dependent fluctuation of the impedance response, implying a comparatively more stable interfacial state during dynamic cycling. Such behavior suggests that the outer N-doped carbon layer may improve electronic conduction at the particle surface and help alleviate polarization and mass-transport limitations during repeated lithiation/delithiation. These operando results are well consistent with the electrochemical trends revealed by the cycling, rate, GITT, and EIS measurements.

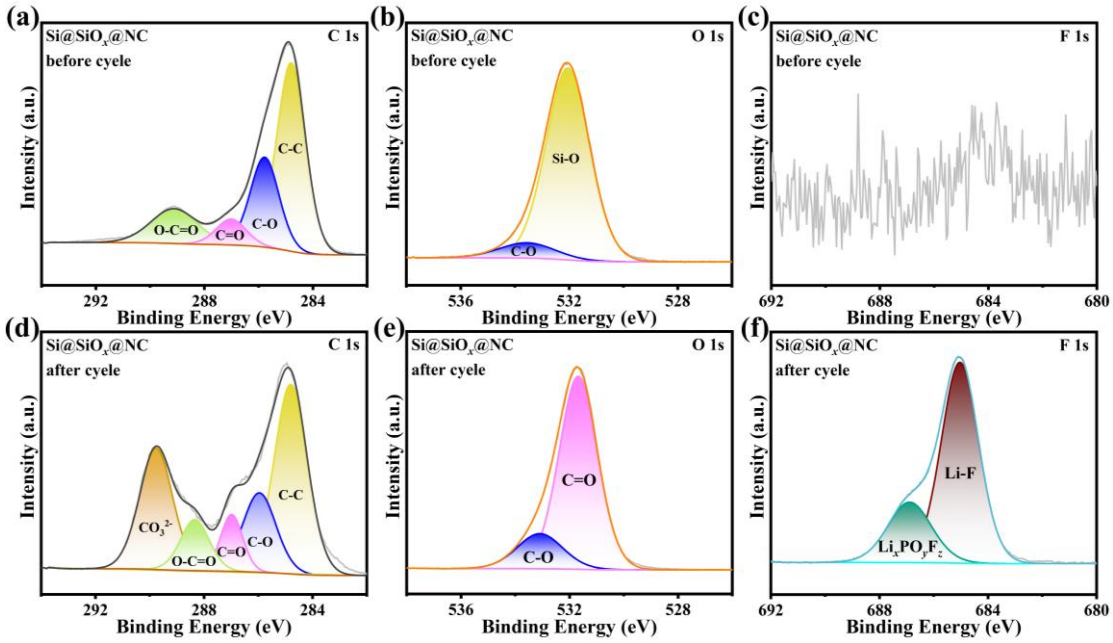


Fig. 10. High-resolution XPS spectra of the Si@SiO$_x$@NC electrode before and after cycling: (a, d) C 1s, (b, e) O 1s, (c, f) F 1s

XPS was employed to probe the surface chemical states of the Si@SiO$_x$@NC electrode before and after cycling, as shown in Fig. 10. Prior to cycling, the C 1s spectrum is dominated by the C-C component at ~284.8 eV, while weaker contributions at higher binding energies can be

assigned to C-O, C=O, and O-C=O species, indicating the presence of a certain amount of oxygen-containing functional groups in addition to the carbon framework. Among them, the O-C=O contribution is more reasonably attributed to intrinsic surface oxygen-containing functionalities, although the presence of a small amount of carboxyl-related species cannot be excluded. The O 1s spectrum before cycling can be mainly deconvoluted into Si-O species together with a minor C-O contribution, suggesting that the electrode surface is still dominated by SiOx-related oxygen environments at this stage. Meanwhile, no obvious characteristic signal is detected in the F 1s region before cycling.

After cycling, the high-binding-energy region of the C 1s spectrum becomes significantly intensified, and a new carbonate-related contribution emerges at around 289-290 eV, indicating the formation of more interfacial products containing O-C=O environments as a result of electrolyte decomposition. Correspondingly, the post-cycling O 1s spectrum is more appropriately assigned to C=O and C-O-related oxygen species within the interphase layer. In combination with the appearance of LiF and fluorophosphate signals in the F 1s spectrum, these results suggest that a surface SEI film is formed after cycling, which is composed of oxygen-containing organic species, carbonate-type components, and decomposition products derived from $LiPF_6$[42, 43].

4. Conclusions

In this work, a Si@SiO_x@NC composite with an outer N-doped carbon shell was successfully fabricated via in situ polymerization of a melamine-assisted resorcinol-

formaldehyde resin followed by carbonization. Structural characterizations demonstrate that the composite retains the crystalline Si core while forming an outer N-doped carbon coating layer. Compared with Si@SiO_x@C, the Si@SiO_x@NC sample exhibits a higher carbon-related content, a larger specific surface area, and a more developed small-mesopore structure. Electrochemical measurements reveal that Si@SiO_x@NC delivers markedly improved lithium-storage performance, maintaining reversible specific capacities of 1022.3 and 938 $mAh \cdot g^{-1}$ after 200 cycles at 0.5 and 1 $A \cdot g^{-1}$, respectively, both of which are significantly higher than those of Si@SiO_x@C. Meanwhile, Si@SiO_x@NC shows a higher initial coulombic efficiency of 74.08% and a superior capacity recovery of 91.5% after high-rate cycling. Combined with the GITT, EIS, and operando impedance analyses, the enhanced electrochemical performance can be attributed to the beneficial role of the N-doped carbon layer in lowering charge-transfer resistance, facilitating Li^+ transport, and alleviating polarization during cycling. In addition, the post-cycling XPS results further suggest the formation of a relatively stable interfacial film on the electrode surface. Overall, the introduction of the outer N-doped carbon shell effectively optimizes the interfacial chemistry and transport properties of the silicon-based composite anode, thereby contributing to improved cycling stability and reaction kinetics.

Acknowledgement

This work is financially supported by the Climbing Program of Helanshan Laboratory (HLS-2025-PDJH-010), the National Natural Science Foundation of China (22269001), and Yinchuan Science and Technology Program-Regional Collaborative Innovation Special Project (2025XT09).

Author contributions

Bowen Li: Writing-review & editing, Methodology, Conceptualization, Formal analysis, Supervision, Funding acquisition, Haidong Xie: Visualization, Hui Tian: Visualization, Kaiyi Chang: Visualization, Haojie Xu: Investigation, Li-Zhang: Visualization, Chang Li: Visualization, Jiao Hou: Investigation, Xingwei Wang: Investigation, Chunping Hou: Data curation, Funding acquisition.

Data availability

The data that support the findings of this study are available on request.

Declarations

The authors declare that they have no conflict of interest.

References

[1] C.K. Chan, H. Peng, G. Liu, K. McIlwrath, X.F. Zhang, R.A. Huggins, Y. Cui, High-performance lithium battery anodes using silicon nanowires, Nature Nanotechnology. 3 (2008) 31-35, http://10.1038/nnano.2007.411.

[2] A. Magasinski, P. Dixon, B. Hertzberg, A. Kvit, J. Ayala, G. Yushin, High-performance lithium-ion anodes using a hierarchical bottom-up approach, Nat Mater. 9 (2010) 353-358, http://10.1038/nmat2725.

[3] H. Wu, G. Chan, J.W. Choi, I. Ryu, Y. Yao, M.T. McDowell, S.W. Lee, A. Jackson, Y. Yang, L. Hu, Y. Cui, Stable cycling of double-walled silicon nanotube battery anodes through solid–electrolyte interphase control, Nature Nanotechnology. 7 (2012) 310-315, http://10.1038/nnano.2012.35.

[4] N. Liu, H. Wu, M.T. McDowell, Y. Yao, C. Wang, Y. Cui, A yolk-shell design for stabilized and scalable li-ion battery alloy anodes, Nano Lett. 12 (2012) 3315-3321, http://10.1021/nl3014814.

[5] W. Liu, J. Wang, J. Wang, X. Guo, H. Yang, Three-dimensional nitrogen-doped carbon coated hierarchically porous silicon composite as lithium-ion battery anode, Journal of Alloys and Compounds. 874 (2021) 159921, http:///10.1016/j.jallcom.2021.159921.

[6] X. Xu, F. Wu, W. Yang, X. Dai, T. Wang, J. Zhou, J. Wang, D. Guo, Silicon@Natural Nitrogen-Doped Biomass Carbon Composites Derived from “Silicon Tofu” as Green and Efficient Anode Materials for Lithium-Ion Batteries, ACS Sustainable Chemistry & Engineering. 9 (2021) 13215-13224, http://10.1021/acssuschemeng.1c03879.

[7] L.Y. Yang, H.Z. Li, J. Liu, Z.Q. Sun, S.S. Tang, M. Lei, Dual yolk-shell structure of carbon and silica-coated silicon for high-performance lithium-ion batteries, Scientific Reports. 5 (2015) 10908,

http://10.1038/srep10908.

[8] M.-G. Jeong, M. Islam, H.L. Du, Y.-S. Lee, H.-H. Sun, W. Choi, J.K. Lee, K.Y. Chung, H.-G. Jung, Nitrogen-doped Carbon Coated Porous Silicon as High Performance Anode Material for Lithium-Ion Batteries, Electrochimica Acta. 209 (2016) 299-307, http://https://doi.org/10.1016/j.electacta.2016.05.080.

[9] J. Zhu, J. Yang, Z. Xu, J. Wang, Y. Nuli, X. Zhuang, X. Feng, Silicon anodes protected by a nitrogen-doped porous carbon shell for high-performance lithium-ion batteries, Nanoscale. 9 (2017) 8871-8878, http://10.1039/C7NR01545C.

[10] C.-H. Jung, J. Choi, W.-S. Kim, S.-H. Hong, A nanopore-embedded graphitic carbon shell on silicon anode for high performance lithium ion batteries, Journal of Materials Chemistry A. 6 (2018) 8013-8020, http://10.1039/C8TA01471J.

[11] J. Ryu, T. Chen, T. Bok, G. Song, J. Ma, C. Hwang, L. Luo, H.-K. Song, J. Cho, C. Wang, S. Zhang, S. Park, Mechanical mismatch-driven rippling in carbon-coated silicon sheets for stress-resilient battery anodes, Nature Communications. 9 (2018) 2924, http://10.1038/s41467-018-05398-9.

[12] Z. Yang, M. Jiang, X. Wang, Y. Wang, M. Cao, Constructing a Stable Si–N-Enriched Interface Boosts Lithium Storage Kinetics in a Silicon-Based Anode, ACS Applied Materials & Interfaces. 13 (2021) 52636-52646, http://10.1021/acsami.1c15483.

[13] Y. Wei, Y. Huang, Y. Zeng, Y. Zhang, W. Cheng, W. Wang, D. Jia, X. Tang, L. Wang, Designed Formation of Yolk-Shell-Like N-Doped Carbon-Coated Si Nanoparticles by a Facile Method for Lithium-Ion Battery Anodes, ACS Applied Energy Materials. 5 (2022) 1471-1477, http://10.1021/acsaem.1c02785.

[14] Z. Lin, J. Li, Q. Huang, K. Xu, W. Fan, L. Yu, Q. Xia, W. Li, Insights into the Interfacial Instability between Carbon-Coated SiO Anode and Electrolyte in Lithium-Ion Batteries, The Journal of Physical Chemistry C. 123 (2019) 12902-12909, http://10.1021/acs.jpcc.9b02509.

[15] M.-Y. Yan, G. Li, J. Zhang, Y.-F. Tian, Y.-X. Yin, C.-J. Zhang, K.-C. Jiang, Q. Xu, H.-L. Li, Y.-G. Guo, Enabling SiO_x/C Anode with High Initial Coulombic Efficiency through a Chemical Pre-Lithiation Strategy for High-Energy-Density Lithium-Ion Batteries, ACS Applied Materials & Interfaces. 12 (2020) 27202-27209, http://10.1021/acsami.0c05153.

[16] H. Zhou, B. Yang, H. Zhou, C. Liu, S. Zhang, T. Feng, Z. Xu, Z. Fang, J. Gao, M. Wu, Carbon Shells and Carbon Nanotubes Jointly Modified SiOx Anodes for Superior Lithium Storage, ACS Applied Energy Materials. 7 (2024) 10307-10316, http://10.1021/acsaem.4c01513.

[17] H. Dong, H. Xie, Q. Song, Z. Ning, Multilayer boron doped Si@SiO_x/C from Si-Ca alloy for lithium-ion battery anodes, Journal of Energy Storage. 90 (2024) 111960, http:///10.1016/j.est.2024.111960.

[18] Z. Yu, B. Wu, X. Yao, X. Wang, W. Lv, N. Zhou, Y. Li, G. Qu, Cobweb-like Porous Architecture Engineering for Silicon-Rich Composite Anode, Journal of Alloys and Compounds. 1014 (2025) 178766, http://10.1016/j.jallcom.2025.178766.

[19] Y. Sun, L. Zhao, N. Mi, J. He, J. Xu, Silicon@Carbon Composite with Bioinspired Root-Nodule Nanostructures as Anode for High-Performance Lithium-Ion Batteries, Molecules. 30 (2025) 4157, http://10.3390/molecules30214157.

[20] B.G. Lee, S.H. Lee, V. Do, J.W. Lee, S.H. Choi, W. Kim, W.I. Cho, Co-synthesis and Electrochemical Investigation of the Nitrogen-Doped Carbon Layer with Metallic Nano Beads on the SiOx Anode for Lithium Secondary Batteries, ACS Applied Materials & Interfaces. 16 (2024) 10042-10051, http://10.1021/acsami.3c16105.

[21] Y. Xiao, Y. Mao, T. Li, X. Hao, W. Wang, Facile Synthesis of a SiO_x-Graphite Composite toward Practically Accessible High-Energy-Density Lithium-Ion Battery Anodes, ACS Applied Materials & Interfaces. 15 (2023) 45938-45948, http://10.1021/acsami.3c11311.

[22] A. Roy, S.B. Mujib, G. Singh, C_{60} Fullerene-Reinforced Silicon Oxycarbide Composite Fiber Mats: Performance as Li-Ion Battery Electrodes, ACS Omega. 9 (2024) 35757-35768, http://10.1021/acsomega.4c04224.

[23] A. Mateen, A.J. Khan, Z. Zhou, A. Mujear, G. Farid, W. Yan, H. Li, J. Li, Z. Bao, Silicon Nanowires via Metal-Assisted Chemical Etching for Energy Storage Applications, ChemSusChem. 18 (2025) e202400777, http://https://doi.org/10.1002/cssc.202400777.

[24] H. Shang, Y. Zhou, H. Li, J. Peng, X. Hao, L. Guo, B. Sun, Solanaceous Crops-Derived Nitrogen-Doped Biomass Carbon Material as Anode for Lithium-Ion Battery, Nanomaterials. 15 (2025) 1357, http://10.3390/nano15171357.

[25] R. Cong, M. Jo, A. Martino, H.-H. Park, H. Lee, C.-S. Lee, Three-dimensional network of nitrogen-doped carbon matrix-encapsulated Si nanoparticles/carbon nanofibers hybrids for lithium-ion battery anodes with excellent capability, Scientific Reports. 12 (2022) 16002, http://10.1038/s41598-022-20026-9.

[26] A. Huang, Y. Tu, Q. Yu, Preparation and electrochemical properties of nitrogen-doped starch hard carbon anode materials for lithium-ion battery, International Journal of Electrochemical Science. 19 (2024) 100774, http:///10.1016/j.ijoes.2024.100774.

[27] Z.D. Zhang, H.P. Zhou, W.D. Xue, R. Zhao, W.J. Wang, T.T. Feng, Z.Q. Xu, S. Zhang, J.X. Liao, M.Q. Wu, Nitrogen-plasma doping of carbon film for a high-quality layered Si/C composite anode, Journal of Colloid and Interface Science. 605 (2022) 463-471, http:///10.1016/j.jcis.2021.06.147.

[28] J. Hwang, M. Jung, J.-J. Park, E.-K. Kim, G. Lee, K.J. Lee, J.-H. Choi, W.-J. Song, Preparation and Electrochemical Characterization of Si@C Nanoparticles as an Anode Material for Lithium-Ion Batteries via Solvent-Assisted Wet Coating Process, Nanomaterials, 2022, p. 1649.

[29] S. Wu, H. Wu, X. Kong, Y. Li, G. Xu, J. Su, J. Huang, G. Wang, X. Ou, In-situ construction of dual-coated silicon/carbon composite anode for fast-charging Li-ion batteries, Chemical Engineering Journal. 502 (2024) 158032, http:///10.1016/j.cej.2024.158032.

[30] X. Guan, Y. Zhang, I. Kinloch, M. Bissett, "Nanoskeleton" Si-SiO_x/C Anodes toward Highly Stable Lithium-Ion Batteries, ACS applied materials & interfaces. 17 (2025) 10580-10592, http://10.1021/acsami.4c18254.

[31] X. Guo, Z. Yang, W. Wang, Y. Zhang, N. Yu, C. Lu, Silicon/carbon nanotubes anode for lithium-ion batteries: Synthesis, interface and electrochemical performance, Surfaces and Interfaces. 48 (2024), http://10.1016/j.surfin.2024.104223.

[32] J. Ou, B. Li, H. Deng, K. Li, H. Wang, A carbon-covered silicon material modified by phytic acid with 3D conductive network as anode for lithium-ion batteries, Advanced Powder Technology. 34 (2023), http://10.1016/j.apt.2022.103891.

[33] X. Lu, P. Xu, W. Song, P. Zhou, M. Liao, G. Zeng, X. Hu, J. Li, M. Zhang, Q. Huang, Z. Su, Dual carbon boosts silicon-based anodes for excellent initial coulombic efficiency and cycling stability of lithium-ion batteries, Journal of Alloys and Compounds. 938 (2023), http://10.1016/j.jallcom.2022.168646.

[34] Y. Tzeng, C.Y. Jhan, G.Y. Chen, K.M. Chiu, Y.C. Wu, P.S. Wang, Hydrogen Bond-Enabled High-ICE Anode for Lithium-Ion Battery Using Carbonized Citric Acid-Coated Silicon Flake in PAA Binder, ACS

Omega. 8 (2023) 8001-8010, http://10.1021/acsomega.2c07830.

[35] H. Xie, C. Hou, Z. Yue, L. Zhai, H. Sun, H. Lu, J. Wu, S. Yang, Y. Ma, Facile synthesis of C, N, P co-doped SiO_x as anode material for lithium-ion batteries with excellent rate performance, Journal of Energy Storage. 64 (2023) 107147, http:///10.1016/j.est.2023.107147.

[36] M. Jia, W. Zhang, X. Cai, X. Zhan, L. Hou, C. Yuan, Z. Guo, Re-understanding the galvanostatic intermittent titration technique: Pitfalls in evaluation of diffusion coefficients and rational suggestions, Journal of Power Sources. 543 (2022) 231843, http://10.1016/j.jpowsour.2022.231843.

[37] A. Thapa, H. Gao, Low-frequency Inductive Loop and Its Origin in the Impedance Spectrum of a Graphite Anode, Journal of The Electrochemical Society. 169 (2022) 110535, http://10.1149/1945-7111/aca364.

[38] J. Huang, Diffusion impedance of electroactive materials, electrolytic solutions and porous electrodes: Warburg impedance and beyond, Electrochimica Acta. 281 (2018) 170-188, http://https://doi.org/10.1016/j.electacta.2018.05.136.

[39] Z. Guo, C. Lu, Z. Liu, N. Wang, Y. An, C. Li, Y. Xu, X. Sun, X. Zhang, K. Wang, Y. Ma, Dynamic analysis of bi-material cathode in lithium-ion battery capacitors by DRT method, Next Materials. 6 (2025) 100462, http:///10.1016/j.nxmate.2024.100462.

[40] K. Pan, F. Zou, M. Canova, Y. Zhu, J.-H. Kim, Comprehensive electrochemical impedance spectroscopy study of Si-Based anodes using distribution of relaxation times analysis, Journal of Power Sources. 479 (2020) 229083, http://https://doi.org/10.1016/j.jpowsour.2020.229083.

[41] C. Plank, T. Rüther, L. Jahn, M. Schamel, J.P. Schmidt, F. Ciucci, M.A. Danzer, A review on the distribution of relaxation times analysis: A powerful tool for process identification of electrochemical systems, Journal of Power Sources. 594 (2024) 233845, http://https://doi.org/10.1016/j.jpowsour.2023.233845.

[42] P.M. Nogales, S. Lee, S. Yang, I. Yang, S.H. Choi, S.-M. Park, J.H. Lee, C.J. Kim, J.-C. An, S.-K. Jeong, Stabilizing the Solid Electrolyte Interphase of SiOx Negative Electrodes: The Role of Fluoroethylene Carbonate in Enhancing Electrochemical Performance, Batteries. 10 (2024) 385, http://10.3390/batteries10110385.

[43] L. Rynearson, C. Jayawardana, M. Yeddala, B.L. Lucht, Improved Performance of Silicon-Containing Anodes with Organic Solvent-Solubilized Lithium Nitrate, Journal of The Electrochemical Society. 170 (2023) 060525, http://10.1149/1945-7111/acdd26.